



Contents lists available at ScienceDirect

Colloids and Surfaces A: Physicochemical and Engineering Aspects

journal homepage: www.elsevier.com/locate/colsurfa

Structural, Third Order Nonlinear and magnetic properties of pristine and Ni-doped CuO nanoparticles: Diluted magnetic semiconductors

P. Soumya Menon^a, Jibi Kunjumon^a, Ayona K. Jose^a, Aleena P.A^a, Manisha Bansal^b, G. Vinitha^c, Tuhin Maity^b, Priya Mary Abraham^d, D. Sajan^{a,*}, Sajan D. George^e

^a Centre for Advanced Functional Materials, Department of Physics, Bishop Moore College, Mavelikara, Alappuzha, Kerala 690110, India

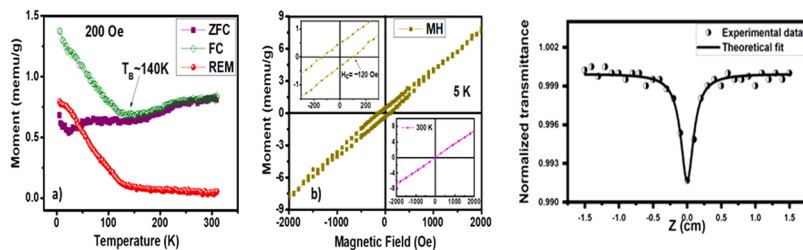
^b School of Physics, Indian Institute of Science Education and Research Thiruvananthapuram, Thiruvananthapuram, Kerala 695551, India

^c Division of Physics, School of Advanced Sciences, Vellore Institute of Technology (VIT), Chennai 600127, India

^d Department of Chemistry, Bishop Moore College, Mavelikara, Alappuzha, Kerala 690110, India

^e Centre for Applied Nanoscience, Department of Atomic and Molecular Physics, Manipal Academy of Higher Education, Manipal 576104, India

GRAPHICAL ABSTRACT



ARTICLE INFO

Keywords:

CuO nanostructures
Optical properties
Nonlinear optical response
Z-scan
Magnetization

ABSTRACT

Ni-doped Copper Oxide nanostructures have been synthesized using the modified auto-combustion method. The structural, morphological, vibrational, linear, and nonlinear optical properties were examined. XRD pattern revealed that the samples exhibited a monoclinic structure having a space group C2/c. Origin of adsorbed oxygen and bivalent state of Cu and Ni were revealed from XPS analysis. HRTEM and FEG-SEM images with EDAX spectra confirmed the formation of spherical particles with smooth surfaces and also validated the purity of synthesized nanostructures. The magnetic measurements confirmed the nanoscale doping of Ni specifically from the superparamagnetic behaviors. The characteristic vibrational modes of CuO were identified from the vibrational analysis. The red-shifted Raman mode with broadening indicates the formation of disorders and size effects. The UV-Visible spectrum showed a decreasing trend in bandgap with an increment in nickel concentration, corresponding to the presence of intra-band defect/imperfection states. Emission peaks obtained from room temperature photoluminescent spectrum indicated the presence of defects in the nanostructures. Third-order nonlinear optical properties, measured via, the Z-scan method with the help of a continuous wave (CW) laser and an enhancement in the nonlinear optical parameters were observed on doping. Hence it confirmed that the prepared nanostructures can be used for various optoelectronic applications.

* Corresponding author.

<https://doi.org/10.1016/j.colsurfa.2022.129582>

Received 18 April 2022; Received in revised form 15 June 2022; Accepted 23 June 2022

Available online 25 June 2022

0927-7757/© 2022 Elsevier B.V. All rights reserved.

1. Introduction

Transition metal oxide (TMOs) nanostructures received enormous interest during recent years in various fields including nonlinear optics [1], spintronics [2][3], energy storage devices [4], and so on, due to their very high surface/volume ratio and excellent physicochemical properties [5]. Among the various TMOs, copper oxide nanoparticles find great attention in various fields such as gas sensing [6], high T_c superconductors [7], magnetic storage devices [8], dilute magnetic semiconductors (DMS) [9], optoelectronics [10], catalysis [11], etc. due to their fascinating properties like low production cost, high chemical stability, higher value of thermal conductivity and environmental friendliness. Copper oxide, which is a p-type semiconductor has attractive antiferromagnetic ordering below its Neel temperature (~ 225 K) (~ 225 K) [12]. According to various reports, the two phases of copper oxide, cuprite (Cu_2O) and tenorite (CuO) are generated from the metal deficient cuprous oxide [13,14]. The tenorite (CuO) phase which belongs to a monoclinic structure with a high value of dielectric constant shows p-type conductivity because of the excess copper or oxygen vacancies at the lattice sites [15]. At the same time, the existence of the Cu phase results in the n-type performance of CuO [15]. Recently CuO nanostructures have been widely used in lithium-ion batteries [16], optical limiters [17], antioxidants [18], giant magneto-resistance [19], solar cells [20], field emitters [21], water splitting [22], etc. Also, the higher values of optical nonlinearities, mechanical strength, and high chemical stability make it as a promising material for nonlinear optical (NLO) applications. The physical and chemical behavior of copper oxide nanostructures can be tailored via doping with various transition metal ions like Ni, Ce, Zn, etc. Ionic radii of Cu^{2+} (0.73 \AA) as well as Ni^{2+} (0.70 \AA) are almost similar, Ni can be doped in the lattice sites of copper oxide without disturbing its crystal structure. The presence of defect states during doping results in the formation of reaction centers in CuO lattice sites [23]. The sol-gel method [24], the hydrothermal method [25], the microwave irradiation method [26], the modified chemical bath deposition [27] and the rapid microwave combustion method [28], etc. were used to prepare Ni-doped CuO nanostructures. Although, such techniques need more energy and high temperature. Therefore, simple and cost effective modified auto combustion technique is used to synthesis Ni doped CuO nanostructures.

According to the literature survey, there were several reports on synthesis methods and characterization techniques of Ni-doped CuO nanostructures. Thangamani et al. studied the magnetic behavior of CuO with Ni doping were prepared using the microwave irradiation technique [29]. Dolai et al. used SQUID magnetometer to investigate the magnetic behavior of nickel-doped CuO [30]. Huang et al. studied the nonlinear optical (NLO) behavior of copper oxide nanoparticles, and estimate their third-order susceptibility between 10^{-12} to 10^{-11} esu cm [31]. Also, the influence of the bandgap of copper oxide nano ellipsoids on its NLO response was investigated by Boltaev et al. [23]. Shahmiri et al. examined the third-order NLO properties of CuO nanosheets with the help of a CW laser of 405 nm [32]. Third-order NLO properties of Ni-doped CuO nanostructures prepared through a modified combustion technique have not yet been reported in any literature. Present work concentrates to investigate the effects of Ni-doped CuO nanostructures of various concentrations, synthesized via a modified auto-combustion method and their structural, morphological, vibrational, magnetic, linear, and nonlinear optical properties were investigated.

2. Experimental methodology

2.1. Synthesis

Nanostructures of pristine and Ni-doped CuO are synthesized using a modified auto combustion method. A stoichiometric amount of cupric acetate (merk, 98% purity) and citric acid (merk, 98% purity) are taken as precursors for the preparation of pristine CuO and cupric acetate,

citric acid, and nickel nitrate hexahydrate for $\text{Cu}_{(1-x)}\text{Ni}_x\text{O}$ ($x = 0.02, 0.04, 0.06$) nanostructures. The mixture is dissolved in deionized water wherein citric acid is used as a fuel. 30 ml of nitric acid is added to the above solution. A solution with no precipitation and sedimentation is obtained after 30 min of stirring. Ammonia is added to maintain the pH as neutral. The solution is heated on a hot plate at about $250 \text{ }^\circ\text{C}$ in the combustion chamber. On the completion of dehydration, internal combustion starts, and a black colored powder is obtained. The resultant powder is heated to about $600 \text{ }^\circ\text{C}$ for 3 hrs in the high-temperature furnace to remove impurities. The sintered samples are taken for different characterizations.

2.2. Instrumentation

Structural analysis of $\text{Cu}_{(1-x)}\text{Ni}_x\text{O}$ were done using powder X-ray diffraction (XRD) method using Bruker D8 Advance X-ray Diffractometer with $\text{Cu} - \text{K}\alpha$ radiation ($\lambda = 1.5406 \text{ \AA}$) having $2\theta = 20 - 80^\circ$. Reitveld refinements of XRD peaks were obtained using FULLPROF studio, version 2. Morphology of synthesized nanostructures was analyzed using HRTEM (Model FEI-TECNAI-G2 SPIRIT-BIO TWIN-TEM 120 kV) and JEOL JSM-7600 F Field Emission Gun -Scanning Electron Microscope (FEG-SEM) and elemental analysis was done using a Supra 35- VP, Carl Zeiss Energy Dispersive Spectroscopy (EDS). The oxidation states and chemical compositions of $\text{Cu}_{(1-x)}\text{Ni}_x\text{O}$ nanostructures were confirmed by X-ray Photoelectron Spectroscopy (XPS) through Thermo Scientific ESCALAB 250 Xi Spectrometer. For vibrational studies, the FT-IR spectra were determined within the spectral region about $4000 - 500 \text{ cm}^{-1}$ by Perkin Elmer Spectrum Fourier Spectrometer and Raman spectra, obtained from 100 to 700 cm^{-1} by Renishaw micro - Raman spectrometer having 30 Mw laser power. The linear optical behavior was evaluated using JASCO V-760 UV-Vis spectrophotometer. The magnetic properties of the samples were investigated using a Physical Property Measurement System (PPMS) for a temperature range of 5 K to 310 K and a $\pm 9 \text{ T}$ loop tracing field. Luminescence property was investigated using a Fluoromax spectrofluorometer with an excitation wavelength of 330 nm . The Z-scan method was used to study the third-order nonlinear optical (NLO) characteristics of $\text{Cu}_{(1-x)}\text{Ni}_x\text{O}$ nanostructures using continuous wave (CW) DPSS laser with 532 nm wavelength.

3. Results and discussion

3.1. Structural and morphological analysis

X-ray diffraction technique is used to analyze phase purity, crystallinity as well as the crystal structure of prepared samples. XRD pattern of $\text{Cu}_{(1-x)}\text{Ni}_x\text{O}$ ($x = 0, 0.02, 0.04, 0.06$) shown in Fig. 1 (a) was recorded in the 2θ range $20 - 80^\circ$. Peaks are observed at $32.25^\circ, 35.25^\circ, 38.43^\circ, 48.44^\circ, 53.17^\circ, 58.0^\circ, 61.28^\circ, 66.01^\circ, 67.92^\circ, 72.20^\circ,$ and 74.93° which corresponds to the planes (110), (-111), (111), (-202), (020), (202), (-113), (-311), (220), (311) and (-222) respectively. The peaks observed are in perfect agreement with JCPDS data (card no. 89 - 5895). There are no other peaks correlating to other phases of Cu are found. XRD profile reveals a monoclinic symmetry with space group C2/c [33]. An additional peak at 43.076° is observed for the samples $\text{Cu}_{0.96}\text{Ni}_{0.04}\text{O}$ and $\text{Cu}_{0.96}\text{Ni}_{0.04}\text{O}$, which corresponds to the (111) cubic phase of NiO [34]. A small peak due to (220) NiO FCC phase appeared in the CuO with a doping concentration of 6% [35]. The intensity of the XRD pattern decreases and peaks shift towards higher theta values with an increase in doping, which confirms the influence of doping percentage on crystal structure, as shown in Fig. 1 (b). Hence, it can be concluded that doping influenced the entire crystallinity of nanostructures even though it did not disturb the monoclinic symmetry. Observed peak shift could be due to the lattice reduction and can be attributed to incorporation of smaller Ni^{2+} (ionic radii = 0.70 \AA) into

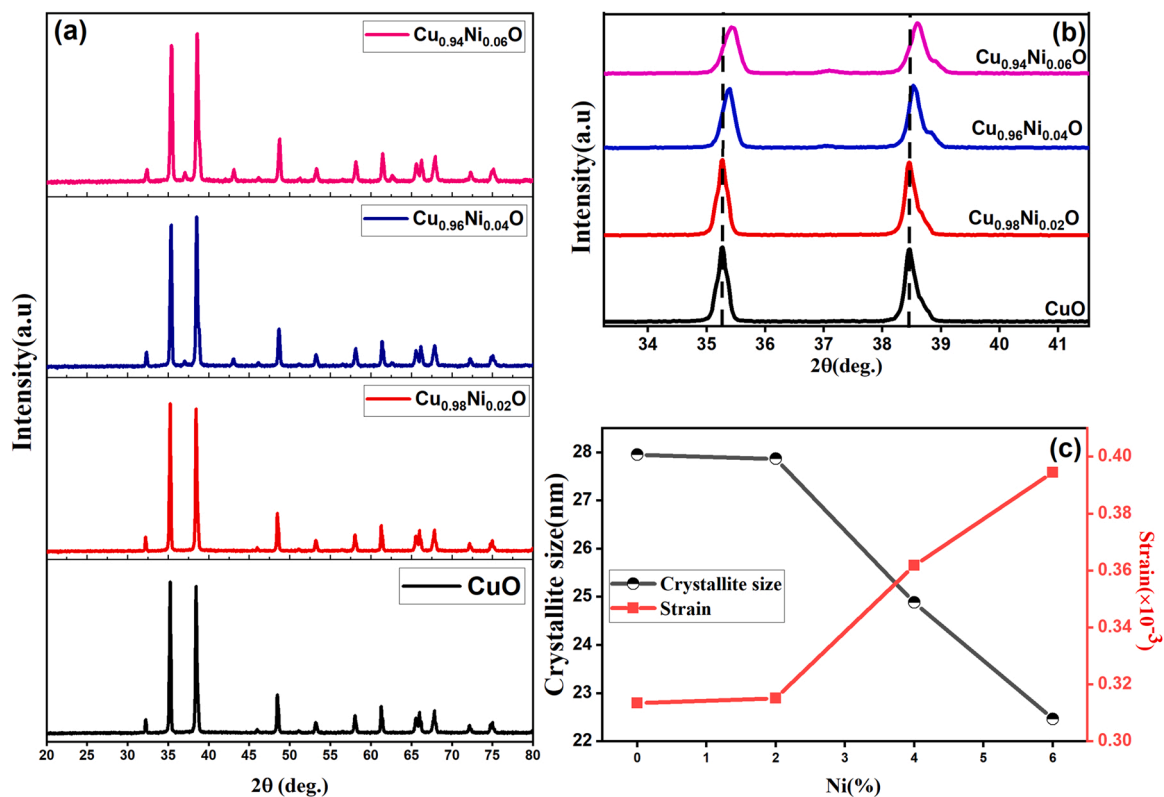


Fig. 1. (a) XRD profile of $\text{Cu}_{(1-x)}\text{Ni}_x\text{O}$ ($x = 0, 0.02, 0.04, 0.06$), (b) Shift in peak, (c) variation in crystallite size and microstrain verses Ni doping percentage.

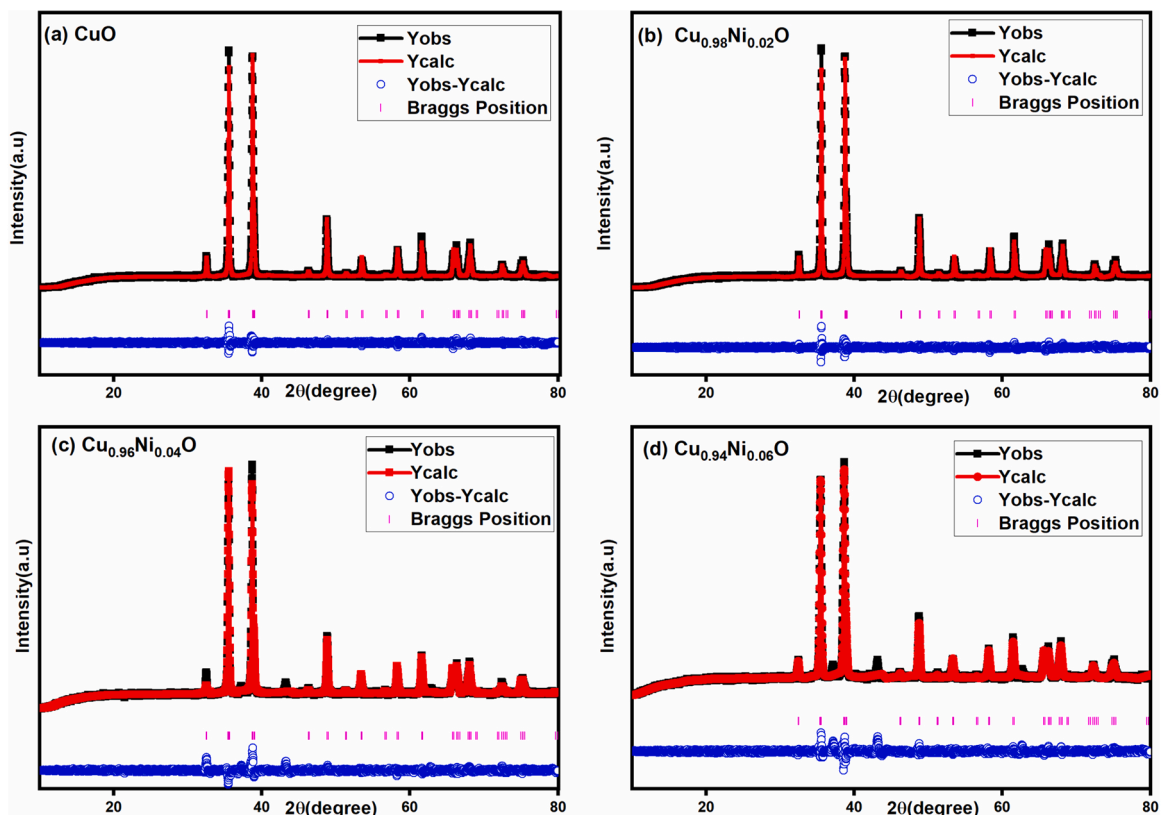


Fig. 2. (a)-(d) Rietveld refinement of $\text{Cu}_{(1-x)}\text{Ni}_x\text{O}$ ($x = 0, 0.02, 0.04, 0.06$) nanostructures.

CuO lattice (ionic radii of $\text{Cu}^{2+} = 0.73 \text{ \AA}$) [34].

The average crystallite size of $\text{Cu}_{(1-x)}\text{Ni}_x\text{O}$ was obtained from the Debye-Scherrer formula,

$$D = \frac{k\lambda}{\beta \cos \theta} \quad (1)$$

where, D stands for average crystallite size, k for shape factor (0.89), λ for wavelength of X-ray for Cu- $k\alpha$ radiation, ($\lambda = 1.5406 \text{ \AA}$), β is the full width at half maximum and θ in degree for diffraction angle. Dislocation density is calculated using average crystallite size using the relation [36].

$$\delta = \frac{1}{D^2} \quad (2)$$

Average crystallite size, dislocation density, Lattice parameters, and strain for pristine as well as doped samples are listed in Table S1. D decreases from 27.951 nm to 22.469 nm on an increase in doping concentration whereas microstrain increases, as shown in Fig. 1 (c). The Rietveld analysis and Le-Bail fit (Fig. 2) confirm the monoclinic structure of $\text{Cu}_{(1-x)}\text{Ni}_x\text{O}$ with space group C2/c. Refined parameters were tabulated in Table S2.

Williamson-Hall analysis is an efficient tool for determining size and strain on broadening by considering FWHM and corresponding Bragg angle [37]. Average crystallite size and microstrain are obtained using Williamson-Hall (W-H) formula given in Eq. (3).

$$\beta \cos \theta = \frac{k\lambda}{D} + 4\epsilon \sin \theta \quad (3)$$

where, β denotes peak width corresponding to plane, θ the Bragg's angle, k is a constant (having value = 0.89), λ the X-ray wavelength (Cu- $K\alpha = 1.5406 \text{ \AA}$), D is the average crystallite size and ϵ is strain experienced in the lattice.

Fig. 3 illustrates the graph of $4 \sin \theta$ vs. $\beta \cos \theta$. From linear fit, the value of slope gives microstrain and that of intercept gives crystallite

size. W-H Plot illustrates a non-zero slope when there exists a strain in the lattice [38]. From Table S3, it is clear that the D is found to be decreased while the doping concentration increased and strain is found to be increased which indicates dislocation in the crystal lattice [39]. When the doping concentration is increased to 6%, the microstrain became negative which represents a compressive strain. It is also noticed that D evaluated by the Scherrer technique is different from the one obtained from the W-H Plot. The impact of strain broadening was not considered in Scherrer's method, which is responsible for this difference [33].

FEG-SEM analysis of $\text{Cu}_{(1-x)}\text{Ni}_x\text{O}$ ($x = 0, 0.02, 0.04, 0.06$) nanostructures in Fig. 4(a)-(d) are made up of spherical shaped particles with smooth surfaces [36]. With an increase in the doping percentage of Ni, particle size decreased and they exhibited enhanced agglomeration. The morphology of the samples remains almost similar even though there is a change in particle size and agglomeration increased. It is reported that high temperature during synthesis can also lead to particle agglomeration, since smaller particles aggregate to become thermodynamically stable [33].

The chemical compositions of the nanostructures are evaluated by using energy dispersive X-ray mapping (Fig. 5). From the EDAX spectra, we confirm the uniform distribution of copper, oxygen, and nickel. The presence of carbon observed in the SEM images is due to the carbon tape used for measurements. Since there is no trace of impurities, the purity of the samples is confirmed. The weight percentage of Cu and O in CuO was 82.63% and 17.37%, respectively. The weight percentage of Ni was observed to be increased by 1.76%, 2.86%, and 4.93%, respectively, for the samples $\text{Cu}_{(1-x)}\text{Ni}_x\text{O}$ ($x = 0.02, 0.04, 0.06$), which is consistent with the stoichiometry. The increase in the atomic percentage of Ni indicates the substitution of Ni at the site of Cu. Fig. 6 illustrates the TEM images of 6% Ni-doped CuO nanoparticles, which helps in evaluating the morphology and size of the nanoparticles. Each particle appears to be spherical in shape with uniform size, which is in good agreement with FE-SEM analysis. The average particle size is observed to be between

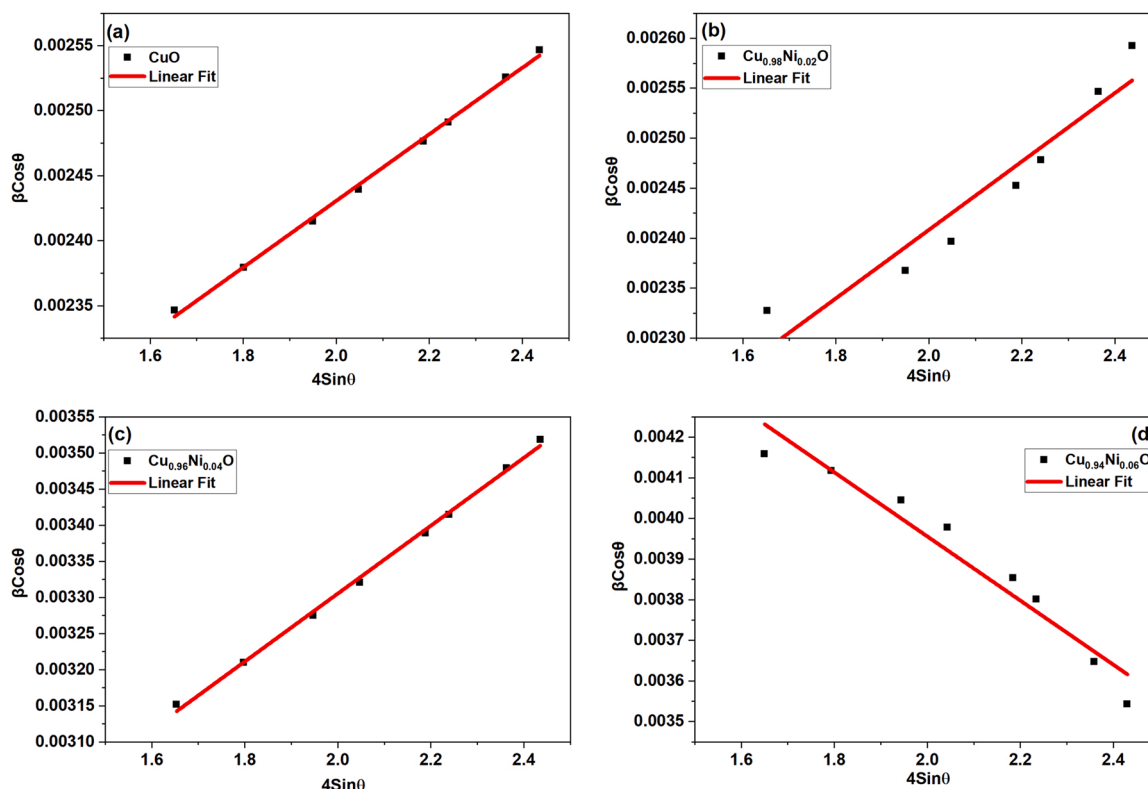


Fig. 3. W-H plot of $\text{Cu}_{(1-x)}\text{Ni}_x\text{O}$ ($x = 0, 0.02, 0.04, 0.06$) nanostructures.

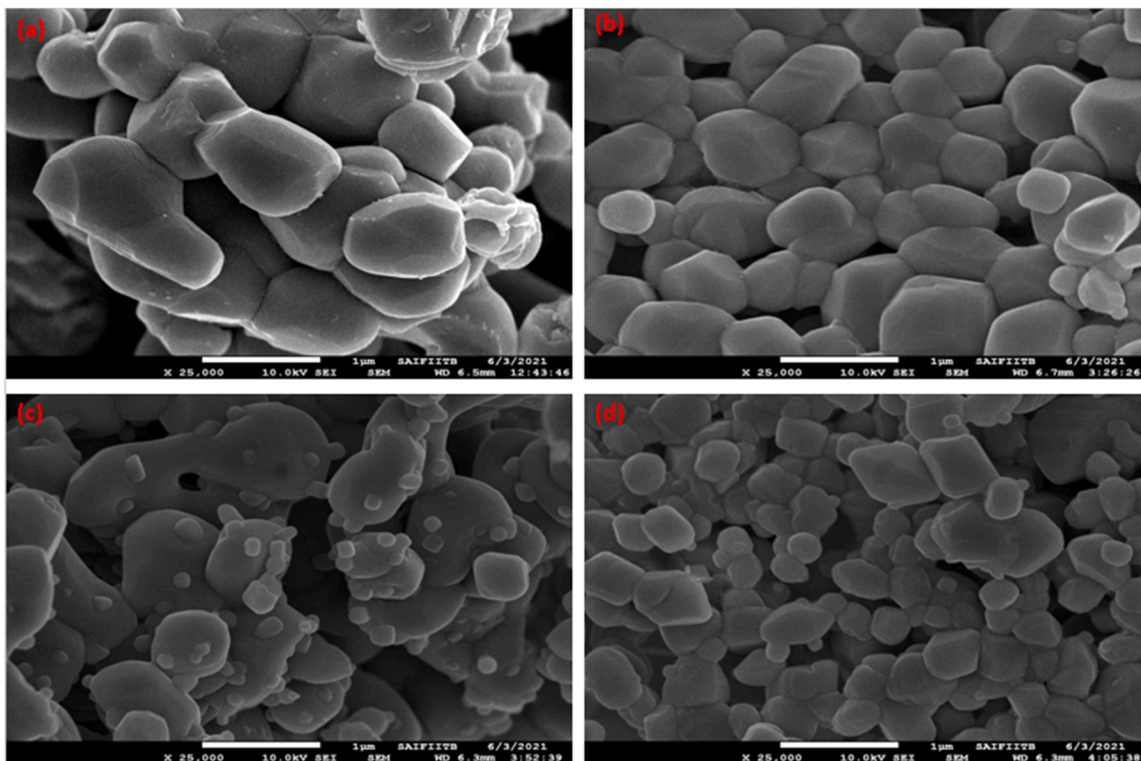


Fig. 4. (a)-(d) FE-SEM images of $Cu_{(1-x)}Ni_xO$ ($x = 0, 0.02, 0.04, 0.06$) nanostructures.

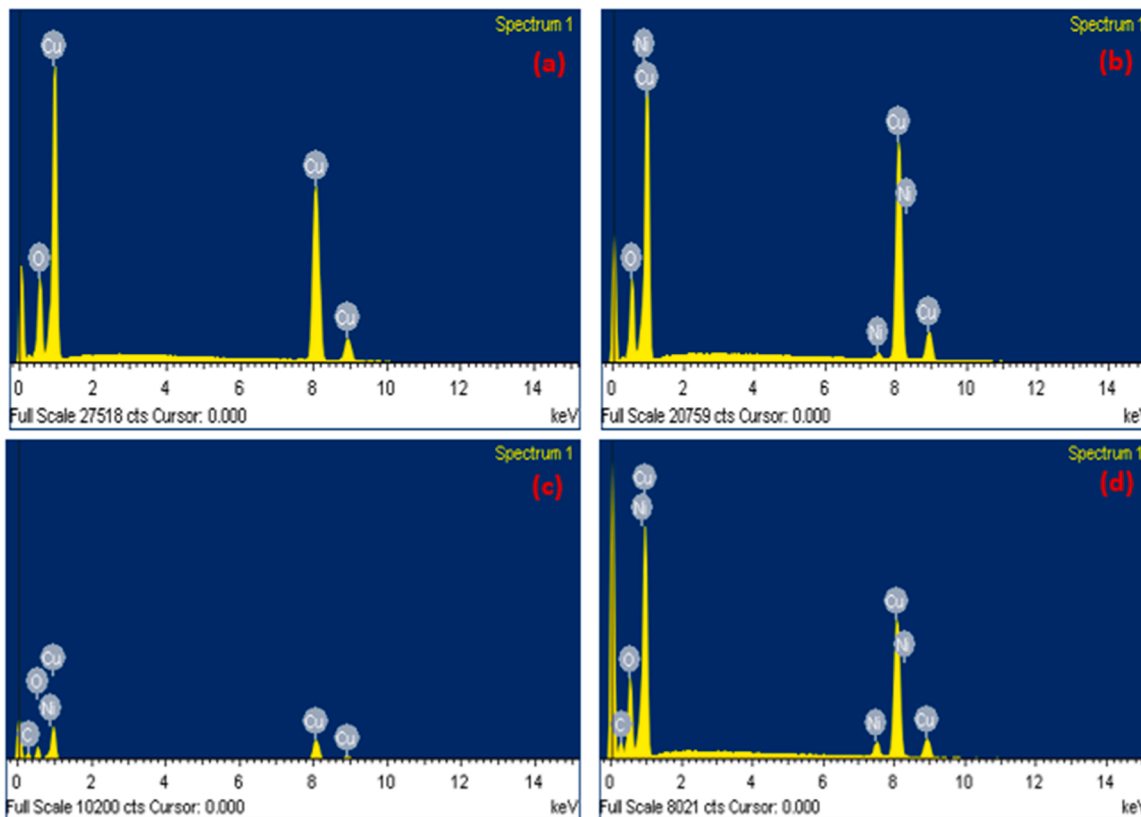


Fig. 5. EDAX of $Cu_{(1-x)}Ni_xO$ ($x = 0, 0.02, 0.04, 0.06$) nanostructures.

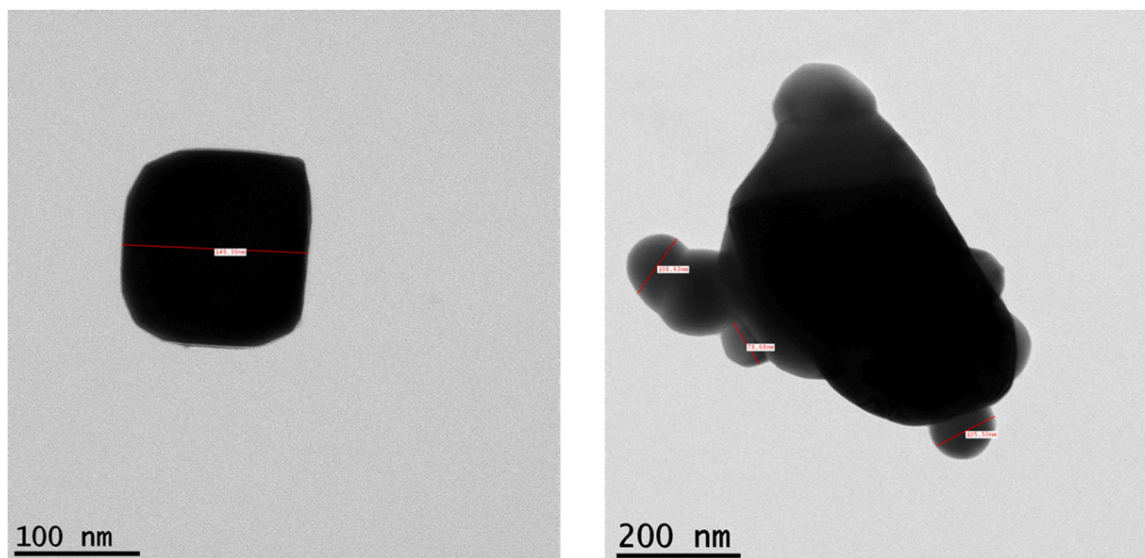


Fig. 6. HR-TEM images of $\text{Cu}_{(1-x)}\text{Ni}_x\text{O}$ ($x = 0.06$) nanostructures.

75 nm and 150 nm.

3.2. Local electronic structure of dopant and defects

XPS study is carried out for analyzing the various oxidation nature of elements along with chemical species, which were occupied on nanostructures surface together with their binding energies [40]. Generally, peak positions in the XPS spectra were highly dependent on the chemical nature of dopants in the host.

Fig. 7 (a) depicts the survey spectrum of pristine with 6% Ni^{2+} doped nanostructure. Ni^{2+} core level spectrum in Fig. 7 (b) gives two main

peaks at 854.14 and 871.72 eV, respectively corresponding to the state $\text{Ni } 2p_{3/2}$ and $\text{Ni } 2p_{1/2}$ and having spin-orbit splitting energy of 17.58 eV [42]. The peak observed at 854.18 eV, attributes to the 2 + oxidation state of Nickel and it is important to mention that the Nickel in the synthesized nanostructures was $\text{Ni } 2p$. Furthermore, the peaks at 860.57 and 880.11 eV denote the satellite peaks of $\text{Ni}2p$ clearly depict Ni^{2+} in the Ni-O bond and also show the formation of $\text{Ni } 2p$ states [40]. The main peaks in core-level spectra of $\text{Cu } 2p$ in CuO and 6% Ni^{2+} doped nanostructure as in Fig. 7 (c) & (d). In Fig. 7 (c), centered at 933.29 and 953.31 eV confirms the formation of CuO . These binding energies are consistent with $2p_{3/2}$ and $2p_{1/2}$ states of Cu^{2+} states and have a

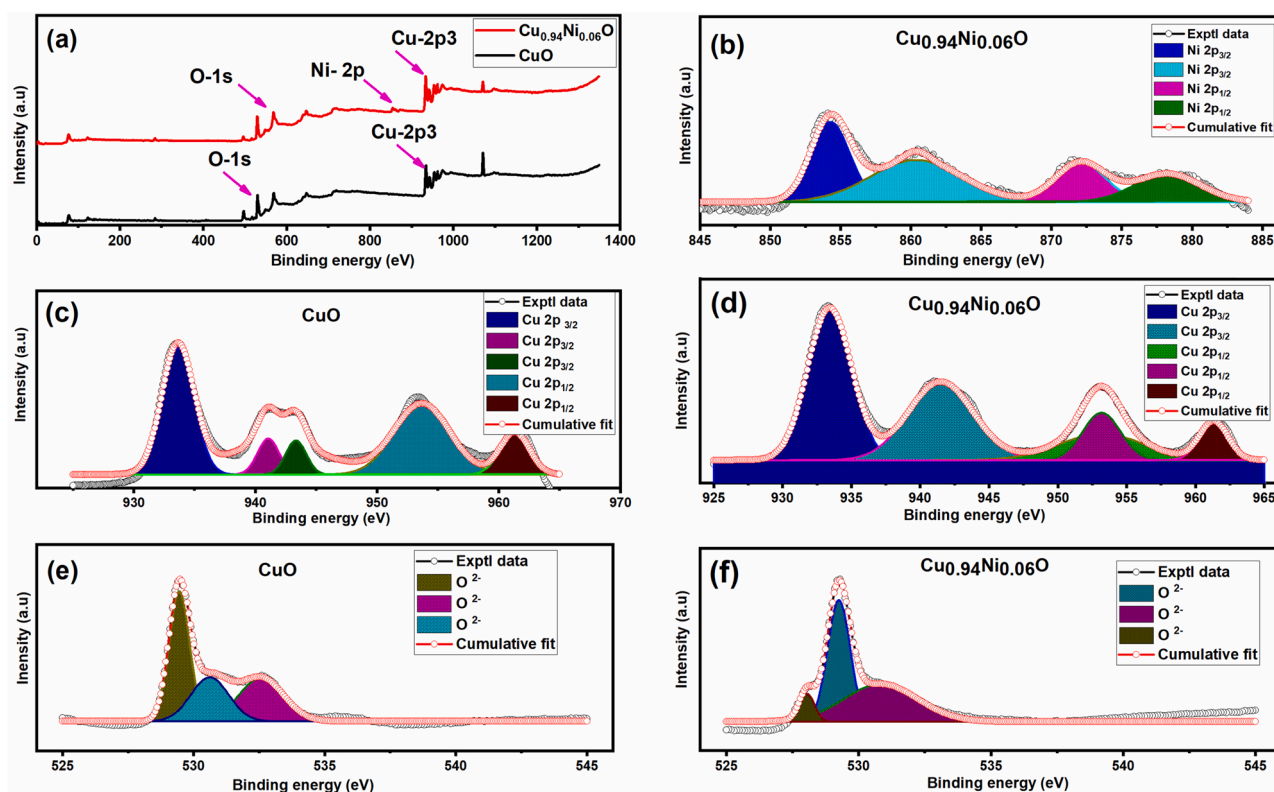


Fig. 7. (a) XPS survey spectrum (b) Core level spectra of nickel (c) & (d) Core level spectra of copper (e) & (f) Core level spectra of oxygen.

spin-orbit splitting of 20.02 eV [41]. Besides, two shorter peaks are observed at 941.88 and 961.89 eV also specify the presence of Cu^{2+} and also denote the $3d^9$ electronic configuration of partially filled d-block of Cu^{2+} [40].

Fig. 7 (e) & (f) denotes the O-1 s spectra of the pristine sample as well as 6% Ni-doped CuO. An asymmetric curve with two well-defined peaks centered at 529.54 and 532 eV is identified for pristine and three peaks at 528, 529, and 532 eV are observed for 6% Ni^{2+} doped CuO. The two peaks in the case of the pristine sample are consistent with Cu-O in CuO lattice and adsorbed oxygen in Cu-O respectively [41]. A significant reduction in the contribution of the peak at 532 eV with an increase in doping level is observed, which revealed a decrement in the number of secondary phases like Cu_2O [42]. The peak at 530 eV and 532 eV were assigned to doubly ionized O^{2-} in CuO lattice and the origin of surface adsorbed oxygen near oxygen vacancies respectively [40].

3.3. Vibrational spectral analysis

Vibrational spectroscopy is an efficient non-destructive tool in determining the structure, especially the microstructure along with the arrangement of each atom in both ordered and disordered lattice [43, 44]. Fig. 8 gives the Raman spectrum of $\text{Cu}_{(1-x)}\text{Ni}_x\text{O}$ ($x = 0, 0.02, 0.04, 0.06$) synthesized via modified combustion method. CuO nanostructure possesses twelve zone center, optical phonon bands, with C_{2h}^6 space group.

According to group theory, the active optical modes [44] are,

$$\Gamma_{Op} = 4A_u + 5B_u + A_g + 2B_g \quad (4)$$

where Γ_{Op} stands for the degree of vibrational freedom and A_u , B_u and A_g , B_g are designated as IR active and Raman active modes respectively. The number and various types of modes like Raman active, IR active, infrared active, and acoustic modes among the 12 optical phonon modes are given in Table S4.

Generally, the peak position, as well as the peak intensity in Raman spectra, depends on different parameters such as the synthesis method, the structure of lattice, grain size, and also the geometry of the as-prepared nanostructure [45]. On increasing the grain size of a nanostructure, the observed Raman peaks will get sharper and stronger [43]. The high intense peak between 275 and 296 cm^{-1} in $\text{Cu}_{(1-x)}\text{Ni}_x\text{O}$ ($x = 0, 0.02, 0.04, 0.06$) CuO corresponds to A_g mode in CuO, the weak band between 330 and 345 cm^{-1} and 604 – 629 cm^{-1} corresponds to B_{1g} and B_{2g} modes respectively. The strong polarization in the lattice makes decrease in the intensity of B_{2g} intensity [43]. These modes are in good agreement with the previous report [46]. Furthermore, some more modes can be observed in CuO nanostructure because of the formation of some intrinsic as well as extrinsic defects [46]. The presence of one additional peak between 1114 and 1135 cm^{-1} is associated with multi-phonon $2B_g$ mode, because of the electronic density variations in x^2-y^2 direction [44]. After Ni doping, the broadening of peaks and peak strength differences can be read in association with the decrease in particle size and also the formation of disorders in the crystal lattice [44]. A broad peak in $\text{Cu}_{0.96}\text{Ni}_{0.04}\text{O}$ and $\text{Cu}_{0.94}\text{Ni}_{0.06}\text{O}$ appeared at 467 – 558 cm^{-1} , endorsing the generation of point defects like interstitials and/or vacancies at higher doping concentrations [46]. Hence the broadening, as well as the downshifting of spectrum towards lower wavenumber detected in all the fundamental peaks, can be explained based on the quantum confinement effect in $\text{Cu}_{1-x}\text{Ni}_x\text{O}$ nanostructure. Current work shows such a shift in the Raman spectra, indicating the development of a significant number of lattice defects like the occurrence of oxygen vacancies with interstitial defect states [47]. There is an explanation based on the reduction in crystallite size generates through disorder in the nanostructure [45]. A convenient explanation regarding the crystallite size and phonon momentum and thereby the shift in the Raman spectra were given by Heisenberg through the uncertainty principle.

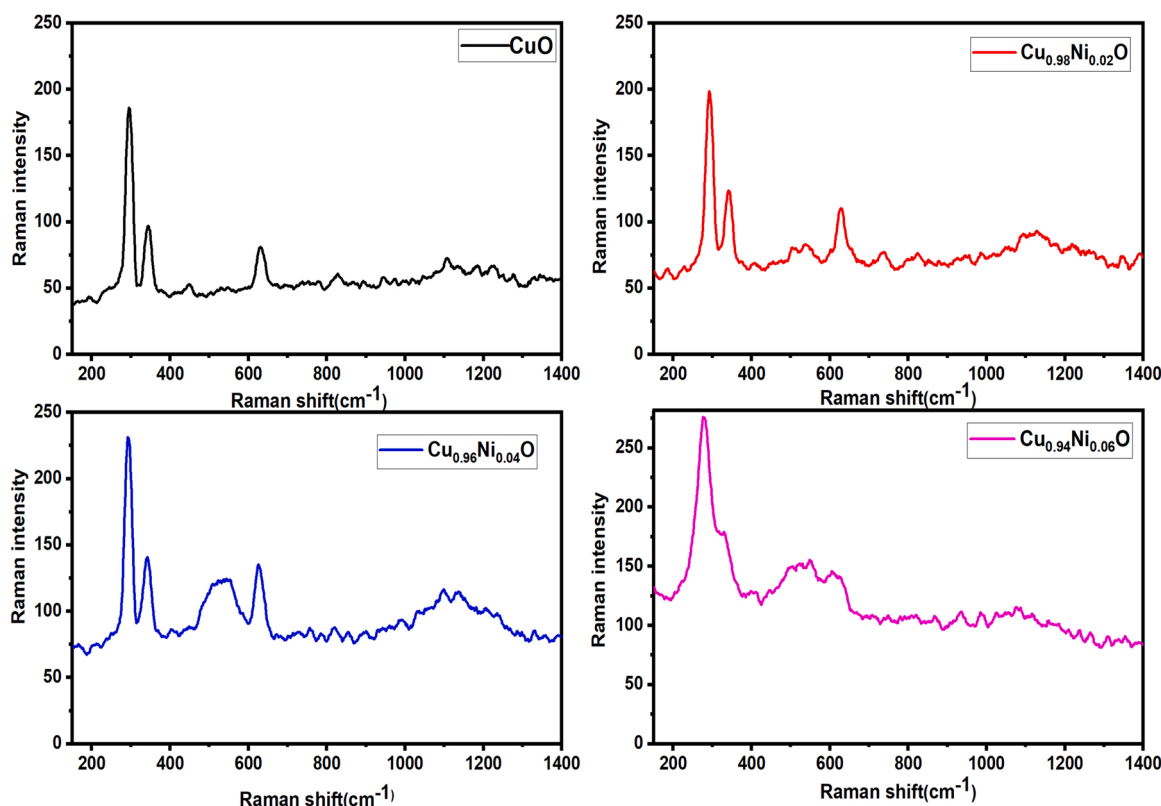


Fig. 8. Raman analysis of $\text{Cu}_{(1-x)}\text{Ni}_x\text{O}$ ($x = 0, 0.02, 0.04, 0.06$) nanostructures.

$$\Delta x \Delta p \geq \frac{h^2}{4} \quad (5)$$

Δx in Eq. (5) stands for the uncertainty in particle size, Δp for phonon momentum distribution, and h for Planks constant. According to this relation, whenever the crystallite size decreases, both the number of phonons confined in a particle along with the degree of phonon momentum distribution gets enhanced. But to achieve the conservation of momentum law, increment in both phonon momentum and scattered phonon momentum has to be done. As a result of such an asymmetric broadening, the Raman bands were shifted towards the lower wavenumber range [45].

FT-IR spectra for $\text{Cu}_{(1-x)}\text{Ni}_x\text{O}$ ($x = 0, 0.02, 0.04, 0.06$) are recorded between the spectral range $500\text{--}4000\text{ cm}^{-1}$ as illustrated in Fig. S1. All the vibrational peaks observed in less than 1000 cm^{-1} can be attributed to the interatomic vibrations of the metal oxide bond [48]. Pure and Ni-doped samples show three active peaks associated with characteristics stretching vibrations of monoclinic CuO, between the wavenumber range 400 cm^{-1} to 600 cm^{-1} . The asymmetric stretching vibrations exhibit the presence of CuO and confirm the deformation vibration of CuO [49]. The peak at 594 and 539 cm^{-1} are related to the stretching vibrations towards the direction of $[-101]$ plane and towards the direction of $[101]$ plane respectively [48]. Meanwhile, the absence of other functional groups of either copper or nickel oxides is identified. Generally, all the absorption peaks in the range $1300\text{--}2000\text{ cm}^{-1}$ are related to physisorbed and/or chemisorbed H_2O with molecules of CO_2 , which are dispersed on the CuO surface [50]. Since the nanostructure possesses a very high ratio in surface area to volume, it absorbs more water content in the atmosphere and exhibits a broad band around 3430 cm^{-1} (adsorbed water molecules) [51]. Moreover, the absence of peak between the wavenumber $605\text{--}660\text{ cm}^{-1}$, which also reflects the absence of Cu_2O infrared active mode, confirms the phase purity or the formation of a single phase of CuO [50].

3.4. Linear optical analysis

Linear optical behavior of synthesized pristine and doped nanostructures can be identified from the UV-Visible absorbance spectrum, from which the classification of electronic transition along with bandgap energy can be evaluated [52]. Absorbance versus wavelength graph of $\text{Cu}_{(1-x)}\text{Ni}_x\text{O}$ ($x = 0, 0.02, 0.04, 0.06$) are illustrated in Fig. 9 (a).

Whenever a semiconductor absorbs incident energy greater than its bandgap energy, the electron from its valence band will shift towards the conduction band and this causes an abrupt increase in the absorbance. Generally, the type of transition depends on absorption coefficient (α) and photon energy ($h\nu$) [51]. If the momentum of the electron is conserved for a transition, then it is said to be a direct transition and on the other hand, if the momentum of the electron is not conserved, then it is called as an indirect transition [51]. As can be seen, the absorption peak of pristine CuO is at 239 nm [53], red-shifted after doping, and designates the incorporation of Ni^{2+} in the lattice of CuO [26]. For direct bandgap materials, like CuO, the (α) and ($h\nu$) are related by the Tauc relation:

$$(\alpha h\nu)^{1/n} = A(h\nu - E_g) \quad (6)$$

where E_g stands for the energy bandgap and n denotes the kind of optical transition, here it is $\frac{1}{2}$. The bandgap energy has been evaluated by plotting $(\alpha h\nu)^2$ and $h\nu$ along the Y and X-axis respectively are given in Fig. 9 (b). By extrapolating the linear section in Fig. 9 (b), the energy bandgap of pristine and doped nanostructures can be calculated and is tabulated in Table 1.

Since the optical properties of a material significantly depend on the value of its bandgap, which in turn depends on crystallite size, morphological properties [46], and the presence of impurities and defects [45]. If the bandgap drastically decreases then the material is considered to be a good conductor and shows better optical properties [53]. Generally, dopant-related states affect the conductivity of the material by creating extra pathways via charge carrier transition [54]. A decrease in bandgap was reported from 3.83 to 3.53 eV in CuO by Srinivasan et al. when it was doped with Zn [53]. Kumar et al. has revealed that the change in the composition of CuO as nickel doping causes the

Table 1
Bandgap energy of $\text{Cu}_{(1-x)}\text{Ni}_x\text{O}$ ($x = 0, 0.02, 0.04, 0.06$) nanostructures.

Sample	Bandgap energy(eV)
CuO	3.81
$\text{Cu}_{0.98}\text{Ni}_{0.02}\text{O}$	3.66
$\text{Cu}_{0.96}\text{Ni}_{0.04}\text{O}$	3.39
$\text{Cu}_{0.94}\text{Ni}_{0.06}\text{O}$	2.23

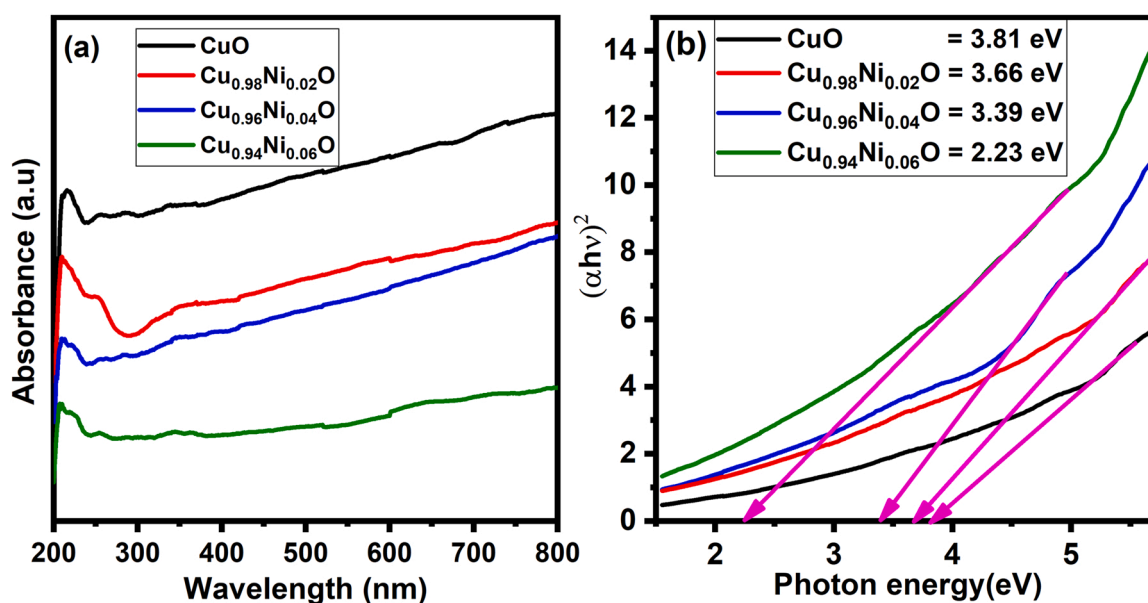


Fig. 9. (a) UV-Visible absorbance plot of $\text{Cu}_{(1-x)}\text{Ni}_x\text{O}$ ($x = 0, 0.02, 0.04, 0.06$) nanostructures and (b) Tauc plot of $\text{Cu}_{(1-x)}\text{Ni}_x\text{O}$ ($x = 0, 0.02, 0.04, 0.06$) nanostructures.

reduction in the bandgap [54]. As doping concentration increases, the bandgap energy decreases. Current work can be explained by the regular substitution of Ni at the site of Cu in the CuO lattice. Such a decrease in E_g on doping can be attributed to the formation of donor density or may be due to the formation of a tail-like effect [55]. The reduction in bandgap from 3.81 to 2.23 eV can be assigned to the tailoring effect of bandgap, evolved by the formation of defects due to copper vacancies [56]. or due to the presence of intra-bandgap-induced defects [54]. Moreover, dopants create some doping energy levels near the valence band and additional holes are generated in the valence band increasing the electrical conductivity [42]. The effect of electronic as well as intrinsic imperfections in CuO was explained by Ovchinnikov et al. The generation of defects or vacancy in CuO nanostructure forms intra-band states in between valence band and conduction band which in turn lead to a decrease in the energy bandgap [54]. Pristine CuO is doped with 2%, 4% and 6% Ni. As a result of doping the structural as well as the optical properties of the prepared nanostructures has changed. A decrease in the bandgap was observed. The schematic representation of the doping mechanism is shown in Fig. 10.

3.5. Photoluminescence spectroscopy

Photoluminescent studies are an effective tool for determining energy levels within the bandgap region which originated from defect sites. It is well known that PL studies are highly sensitive, especially regarding synthesis methods. Room-temperature PL spectra of the samples $\text{Cu}_{(1-x)}\text{Ni}_x\text{O}$ ($x = 0, 0.02, 0.04, 0.06$) is recorded in the range 400 – 640 nm and is shown in Fig. 11. Samples excited at 330 nm exhibit emission peaks in the blue-green region. Three major peaks are observed at 448, 466, 540 nm. Weak peaks are obtained at 436, 481, and 491 nm. The intensity of the PL bands increased with doping concentration which indicates the increase in defects [28]. Observed emissions indicate various luminescent centers including defect energy levels produced from copper, oxygen vacancies, and copper interstitials [56]. Siddiqui et al. explained that defect levels like copper vacancy and oxygen interstitial donate free electrons to the conduction band which will eventually lead to emission. Devi et. al, reported that a blue emission near 470 nm represents the defect-associated emission otherwise it can be caused by the appearance of intrinsic defects or oxygen vacancies [33]. In this study, defect-related emission is observed at 466 nm and the weak peak observed around 481 nm corresponds to the vacancy along with interstitial oxygen [57]. The emission peak at 491 nm originates from the presence of deep-level defects [58]. Xinhong Zhao et al, reported that the radiative recombination among the donor and acceptor level defect centers leads to emission at 436 nm [58]. Similar peaks at $\sim 436, 448,$ and 465 nm are observed and reported by Xinhong Zhao et.al [58]. Green emission located around 540 nm is because of the presence of singly ionized oxygen vacancies [33].

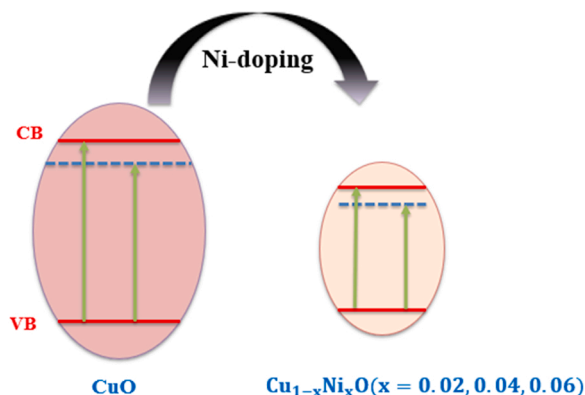


Fig. 10. Doping mechanism in $\text{Cu}_{1-x}\text{Ni}_x\text{O}$ ($x = 0, 0.02, 0.04, 0.06$).

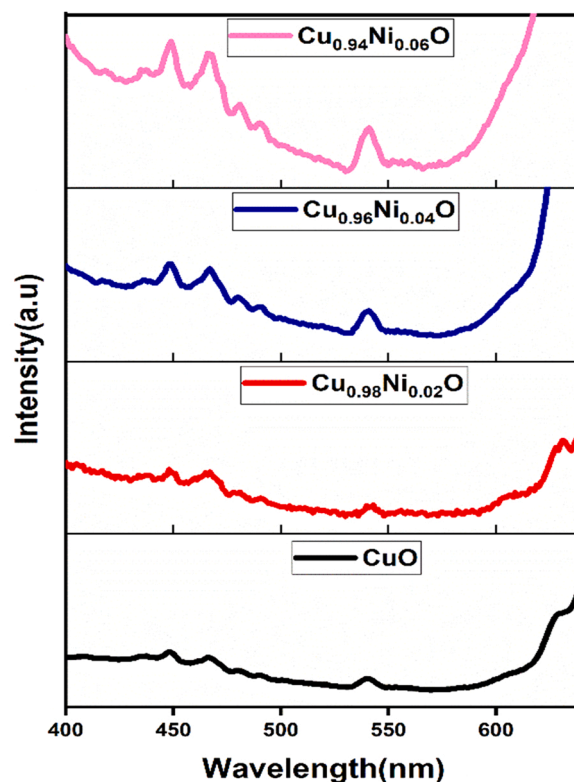


Fig. 11. Photoluminescent spectral analysis of $\text{Cu}_{(1-x)}\text{Ni}_x\text{O}$ ($x = 0, 0.02, 0.04, 0.06$) nanostructures.

3.6. Z-scan measurements under continuous-wave laser

The third-order (NLO) properties like nonlinear absorption (NLA) and nonlinear refractive index (n_2) are determined by a simple and well-known Z-scan technique proposed by Sheik Bahae et al. [59]. The NLO measurements of pristine and Ni-doped copper oxide nanostructures are examined using a continuous-wave diode-pumped solid-state laser (CW-DPSS) with 532 nm wavelength as an excitation source having an output power of about 100 mW. The focal length of the lens used and beam waist (ω_0) at the focal point are about 130 mm and $0.27 \mu\text{m}$ respectively. The aperture size used for closed aperture scanning is 1 mm. At a certain distance, an aperture is placed with a detector behind it. The aperture causes only the central region of the cone of light to reach the detector. Typically aperture size is so chosen so that the values of the normalized transmittance are between 0.1 & 0.5. All the prepared samples are dispersed in an appropriate amount of ethylene glycol because it provides high stability to the sample for Z-scan measurements due to its highly viscous nature. Also, the chosen solvent does not possess any nonlinearity under laser irradiation [23]. Therefore, the samples are dispersed in the solvent and ultrasonicated for 10 min, and then transferred to a quartz cuvette of 1 mm. This was then fixed on a conversion stage that moves through Z-axis and thereby resultant transmittance is calculated by a detector in the presence and absence of an aperture for closed and open z-scan modes respectively [60]. Linear transmittances of prepared samples are about 60–65%. Laser beam intensity at $Z = 0$ (focus) and radius of the aperture is about $0.01488 \text{ (MW/cm}^2\text{)}$ and 1.5 mm respectively and its Rayleigh length is estimated to be about 1.22 mm which obeys the equation $Z_r > L$, L denotes path length. Fig. 12 (a-d) shows the nonlinear absorption coefficient (NLC) of $\text{Cu}_{(1-x)}\text{Ni}_x\text{O}$ nanostructures obtained from open aperture Z-scan curves. For all samples, there is a dip in transmittance value at focus ($z = 0$). This valley-like pattern represents reverse saturation absorption (RSA) behavior and its experimental data is fitted using the relation- [23].

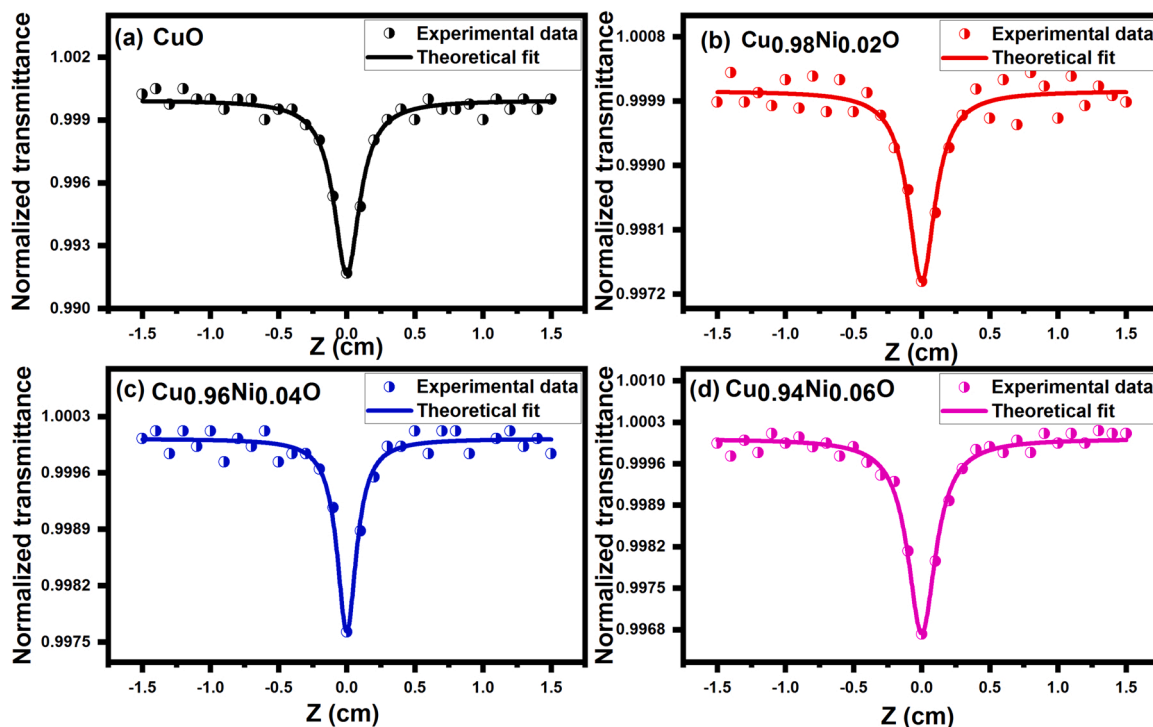


Fig. 12. (a-d): Open aperture z-scan curve of $\text{Cu}_{(1-x)}\text{Ni}_x\text{O}$ ($x = 0, 0.02, 0.04, 0.06$) nanostructures.

$$T(Z) = \frac{1 - \beta I_0 L_{\text{eff}}}{2\sqrt{2} (1 + Z^2/Z_0^2)} \quad (7)$$

$$L_{\text{eff}} = \frac{(1 - e^{-\alpha L})}{\alpha} \quad (8)$$

where, $T(Z)$ denotes the normalized transmittance from open aperture Z-scan measurements, β denotes the nonlinear absorption coefficient, L_{eff} for the effective length of the sample which is given by,

where, L denotes the thickness of the cuvette [61]. n_2 and third order susceptibility of synthesized nanostructures can be determined through closed aperture Z-can curves, as illustrated in Fig. 13 (a-d). All samples shows a pre focal peak followed by a post focal valley, which represents

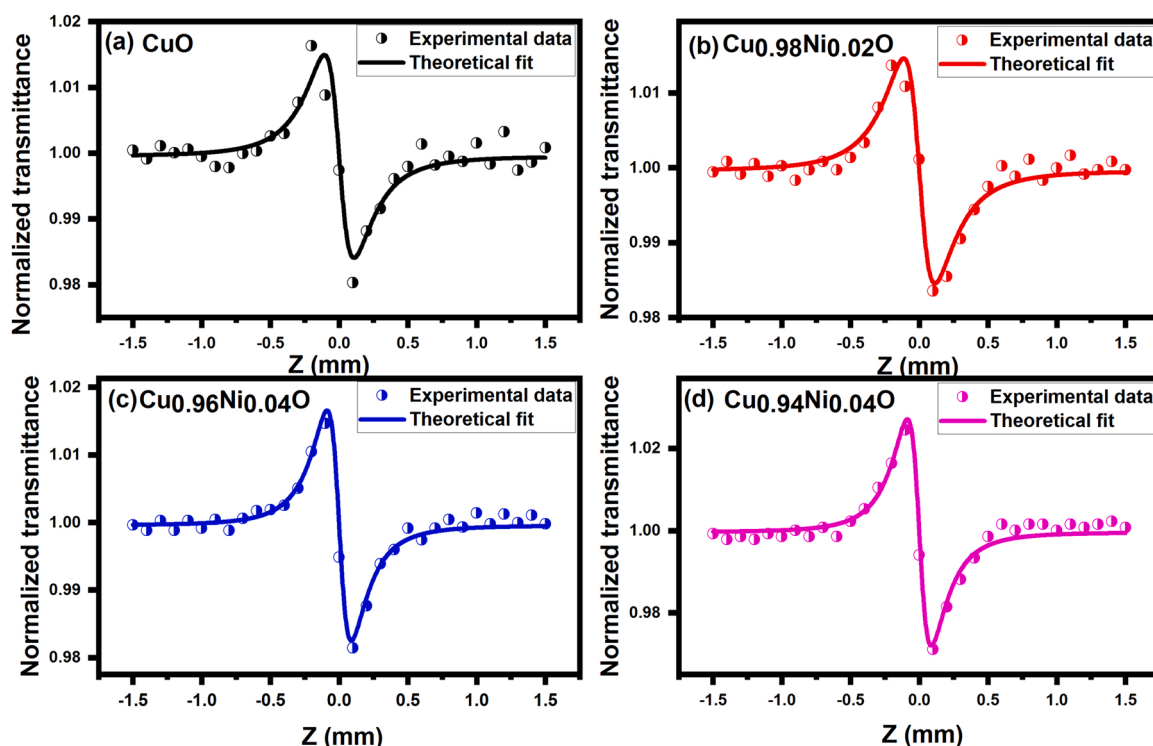


Fig. 13. (a-d): Closed aperture z-scan curve of $\text{Cu}_{(1-x)}\text{Ni}_x\text{O}$ ($x = 0, 0.02, 0.04, 0.06$) nanostructures.

self-defocusing behavior of nanostructures or a negative value of n_2 [60]. Nonlinear refraction in semiconductor nanostructures can be described using different mechanisms like excited state refraction, electronic polarization, free carrier refraction, thermal effects, etc. Under continuous-wave laser irradiation, nonlinear refraction occurs through cumulative thermal heating that occurs in an absorbing medium. Therefore, in the present case under the continuous laser regime, individual atoms get thermally disturbed and act as heating centers. That is, when a laser beam is continuously irradiated on an absorbing medium, a local change in refractive index arises on temperature which produces thermal nonlinearity and leads to both thermal lensing and birefringence [62]. Experimental data are fitted theoretically using the relation,

$$T(Z) = \frac{1 - 4x\Delta\phi_0}{(x^2 + 9)(x^2 + 1)} \quad (9)$$

where, $x = \frac{Z}{Z_0}$, $T(Z)$ denotes normalized transmittance for closed aperture Z-scan mode and $\Delta\phi_0$, on-axis phase shift. Nonlinear refraction and nonlinear absorption coefficients are relevant to evaluate the real ($\text{Re } \chi^{(3)}$) and imaginary ($\text{Im } \chi^{(3)}$) parts of nonlinear susceptibilities. n_2 can be calculated using Eq. (10),

$$n_2 = \frac{\Delta\phi_0\lambda}{2\pi L_{\text{eff}} I_0} \quad (10)$$

$$\chi_{(\text{real})}^{(3)} \text{ (esu)} = 10^{-4} \frac{\epsilon_0 c^2 n_0^2}{\pi} \beta \text{ (cm}^2/\text{W)} \quad (11)$$

$$\chi_{(\text{imaginary})}^{(3)} \text{ (esu)} = 10^{-2} \frac{\epsilon_0 c^2 n_0^2 \lambda}{4\pi^2} \beta \text{ (cm}^2/\text{W)} \quad (12)$$

where, ϵ_0 denotes permittivity in free space and c denotes the velocity of light [63]. Obtained values of nonlinear parameters are in Table 2 and it is observed that, as doping concentration increases, the values of nonlinear optical parameters also tend to increase. This is because of the formation of defect states on lattice sites of copper oxide, which is enhanced during Ni doping. Table 3 represents a comparative analysis of NLO parameters like β and n_2 of previously reported CuO. The enhanced values of β and n_2 reveal that the prepared $\text{Cu}_{(1-x)}\text{Ni}_x\text{O}$ nanostructures can be considered as potential materials for various NLO applications like optical limiting, optical storage, wide tunable lasers etc. [64].

The observed decrease in transmittance near focus designates the Reverse Saturation Absorption (RSA). The NLA behavior of the prepared nanostructure is given by a five-level diagram as shown in Fig. 14. Here the dotted line denotes the non-radiative transition and the straight line denotes the radiative transition. RSA will occur when the absorption cross-section of the excited state (σ_{exe}) is higher than the ground state (σ_{gs}). Depending on the intensity of the input radiation and wavelength, NLA occurs by any of the processes like.

1. From the ground state G_0 to the first singlet excited state E_1 and then to the first triplet state K_1 via inter system crossing (ISC)
2. A direct absorption from the G_0 to the highest excited state E_n (two-photon absorption-2PA)
3. Absorption from E_1 to E_n (Excited State Absorption-ESA)

Table 2

Nonlinear optical parameters of $\text{Cu}_{(1-x)}\text{Ni}_x\text{O}$ ($x = 0, 0.02, 0.04, 0.06$) nanostructures.

Sample code	n_0	n_2 (cm ² /W)	$\beta \times 10^{-4}$ (cm/W)	Re $\chi^{(3)}$ Esu	Im $\chi^{(3)}$ esu	$\chi^{(3)} \times 10^{-8}$ esu
CuO	1.4445	2.104	0.086	2.562×10^{-8}	1.225×10^{-8}	2.840
$\text{Cu}_{0.98}\text{Ni}_{0.02}\text{O}$	1.5251	2.835	0.182	3.165×10^{-8}	1.316×10^{-8}	3.428
$\text{Cu}_{0.96}\text{Ni}_{0.04}\text{O}$	1.3274	3.013	0.172	3.539×10^{-8}	1.471×10^{-8}	3.833
$\text{Cu}_{0.94}\text{Ni}_{0.06}\text{O}$	1.4129	3.446	0.192	4.053×10^{-8}	1.921×10^{-8}	4.485

Table 3

NLO parameters of previously reported CuO [using DPSS ($\lambda = 532$ nm)/ He-Ne (632.8 nm) CW-laser].

Sample details	β (cm/W)	n_2 (cm ² /W)	Ref.
Copper oxide (CuO) nanosheets	0.011×10^{-6}	-0.05×10^{-11}	[32]
5 wt% Cd-doped CuO-PVA nanocomposites	11.0×10^{-6}	38.9×10^{-5}	[65]
15 wt% PVA/TiO ₂ , CuO filled nanocomposites	3.26×10^{-4}	-1.38×10^{-8}	[66]
Sr-CuO-PVA nanocomposite thin films.	4.54×10^{-6}	31.3×10^{-5}	[67]

4. Absorption from the first triplet state K_1 to the highest triplet state K_n .

Hence in the present case, third-order NLA behavior is mainly due to the ESA-assisted RSA can be considered as the reason for the third-order nonlinearity in prepared nanostructures.

3.7. Magnetic measurements

Magnetic measurements of the nanoparticles $\text{Cu}_{0.94}\text{Ni}_{0.06}\text{O}$ are carried out using a PPMS magnetometer. An appropriate demagnetization protocol was followed in which the sample was kept in an oscillation mode sequence from high field to zero field to remove the stray fields from the system [68]. Magnetization measurements (MT) as a function of temperature are done utilizing ZFC (zero-field cooled), FC (field cooled), and remanence measurement protocols (shown in Fig. 15 (a)). After demagnetization, the temperature (T) is ramped down from 310 K to 5 K under no bias field and the moment is measured while warming up from 5–310 K at a low field of 200 Oe for ZFC. Then, the moment is measured again while cooling down from high temperature ~ 310 K to low temperature ~ 5 K for FC measurement under the same field of 200 Oe. Finally, the field is removed and the moment is measured to evaluate the remanence in the sample. A split at blocking temperature (T_B) ~ 140 K is seen between the ZFC and FC curves signifying a phase transition at this temperature. Remanence is also found only below $T_B \sim 140$ K and it increases with decreasing T . Therefore, ferromagnetism (FM) is detected at low temperatures, less than $T_B \sim 140$ K. Above $T_B \sim 140$ K no ferromagnetism is observed.

Further, magnetic hysteresis measurements are done under a maximum applied field of 9 T. A hysteresis loop is observed at a low temperature ~ 5 K (Fig. 15 (b)) with a coercivity of ~ 120 Oe (top inset of Fig. 15 (b)) with a saturation field of ~ 1200 Oe (where loop opening vanishes). A paramagnetic-like behavior is observed for temperatures (~ 300 K) higher than the transition temperature (refer to the bottom inset of Fig. 15 (b)). Hence, the $\text{Cu}_{0.94}\text{Ni}_{0.06}\text{O}$ nanoparticles behave as superparamagnetic nanoparticles with blocking temperature $T_B \sim 140$ K.

4. Conclusions

$\text{Cu}_{(1-x)}\text{Ni}_x\text{O}$ ($x = 0, 0.02, 0.04, 0.06$) nanostructures, synthesized using the modified auto-combustion method exhibit a monoclinic structure from the XRD pattern and are not altered even after Ni doping. The doping of Ni in lattice sites gives rise to a peak shift and thereby shows a decrement in crystallite size with an enhancement in

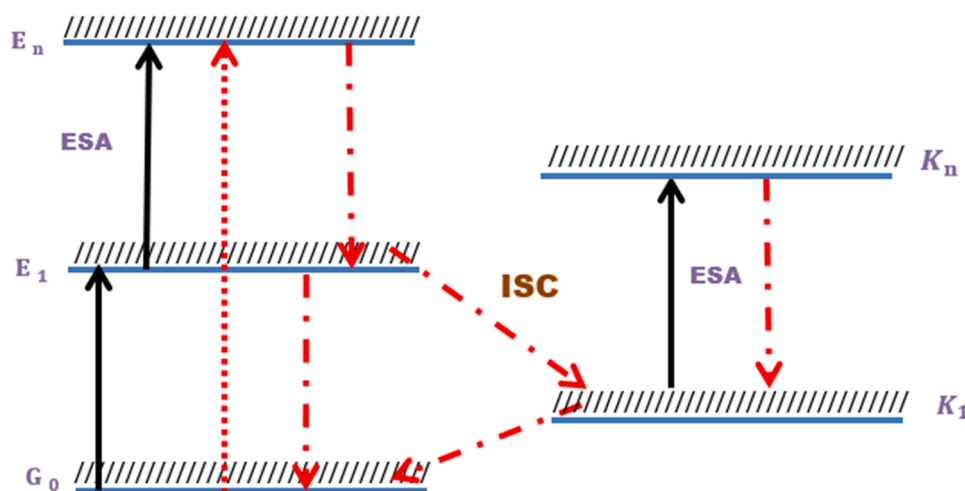


Fig. 14. Five level energy model of $\text{Cu}_{(1-x)}\text{Ni}_x\text{O}$ ($x = 0, 0.02, 0.04, 0.06$) nanostructures.

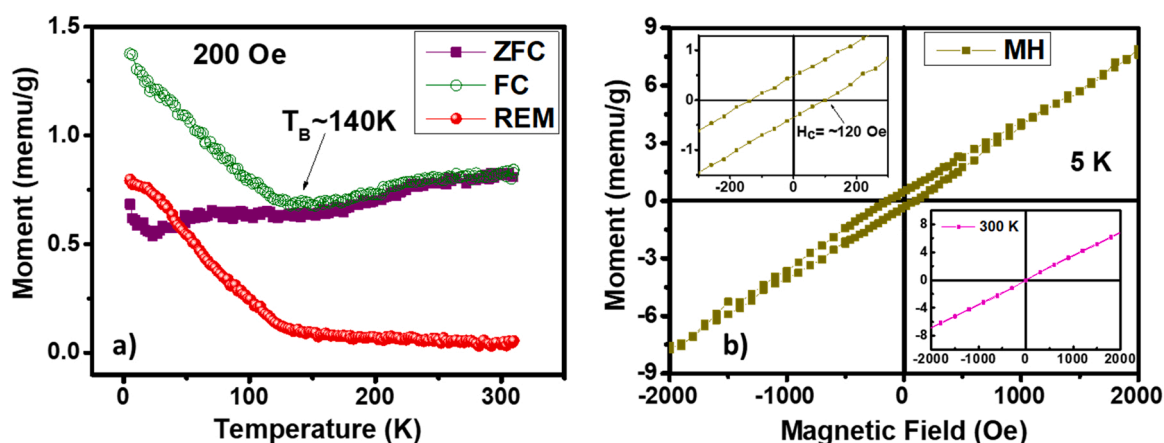


Fig. 15. (a): ZFC, FC and Remanence *MT* measurements for $\text{Cu}_{0.94}\text{Ni}_{0.06}\text{O}$ at 200 Oe field. (b): *MH* measurements at 5 K. Top inset: Zoomed version of *MH* at 5 K to estimate the coercivity. Bottom inset: *MH* at 300 K.

strain. The spherical particles observed from the FEG-SEM get agglomerated as doping concentration increases and the weight percentages of elements are verified from EDAX spectra. From HRTEM images of nanoparticles, spherical shape is confirmed. XPS spectra revealed the presence of adsorbed oxygen and the presence of bivalent states such as Cu^{2+} and Ni^{2+} in the lattice. The broadening of peaks and increase in its intensity along with the Raman shift can be read in association with the decrease in particle size, the origin of disorders in the crystal, and also the occurrence of oxygen vacancies with interstitial defect states. The details from the magnetic measurements show the superparamagnetic behavior of the $\text{Cu}_{(1-x)}\text{Ni}_x\text{O}$ nanoparticles with blocking temperature well below room temperature ($T_B \sim 140$ K for $\text{Cu}_{0.94}\text{Ni}_{0.06}\text{O}$). This confirms the nanoscale doping of Ni. Meanwhile, an asymmetric stretching vibration in FT-IR spectra shows the presence of CuO and confirms its deformation vibration. Bandgap variations calculated by UV-Visible spectroscopy from a range of 3.81–2.23 eV on doping can be related to the formation of intra-band states within the bandgap region, caused by the formation of copper vacancy due to defects along with some donor density levels. The room temperature photoluminescence spectra exhibit emissions in the blue-green region, which is related to the defect in the sample. The third-order nonlinear optical studies using the Z-scan method reveal that both CuO and Ni-doped CuO possess reverse saturation absorption and self-defocusing effect under open and closed aperture Z-scan methods respectively. Also, an increase in the NLO parameters was confirmed on Ni doping.

Hence, $\text{Cu}_{(1-x)}\text{Ni}_x\text{O}$ ($x = 0, 0.02, 0.04, 0.06$) nanostructures can be used for various optical limiting applications.

CRediT authorship contribution statement

P. Soumya Menon: Conceptualization, Investigation, Methodology, Resources, Writing – original draft, Writing – review & editing. **Jibi Kunjumon:** Conceptualization, Investigation, Methodology, Resources, Writing – original draft, Writing – review & editing. **Ayona K. Jose:** Conceptualization, Investigation, Methodology, Resources, Writing – original draft, Writing – review & editing. **Aleena P.A:** Conceptualization, Investigation, Methodology, Resources, Writing – original draft, Writing – review & editing. **Manisha Bansal:** Conceptualization, Investigation, Methodology, Resources, Writing – original draft, Writing – review & editing. **G. Vinitha:** Conceptualization, Investigation, Methodology, Resources, Writing – original draft, Writing – review & editing. **Tuhin Maity:** Conceptualization, Investigation, Methodology, Resources, Writing – original draft, Writing – review & editing. **Priya Mary Abraham:** Conceptualization, Investigation, Methodology, Resources, Writing – original draft, Writing – review & editing. **D. Sajan:** Conceptualization, Investigation, Methodology, Resources, Writing – original draft, Writing – review & editing. **Sajan D. George:** Conceptualization, Investigation, Methodology, Resources, Writing – original draft, Writing – review & editing.

Declaration of Competing Interest

The authors declare that they have no known competing financial interests or personal relationships that could have appeared to influence the work reported in this paper.

Data Availability

Data will be made available on request.

Acknowledgments

Authors acknowledge KSCSTE SARD (File No. 004/SARD/2015/KSCSTE) and DST-FIST (SR/FST/College-182/2013, November 2013 & FIST No. 393 dated 25-09-2014) college scheme at Bishop Moore College Mavelikara for financial support.

Appendix A. Supplementary material

Supplementary data associated with this article can be found in the online version at [doi:10.1016/j.colsurfa.2022.129582](https://doi.org/10.1016/j.colsurfa.2022.129582).

References

- J.W. You, S.R. Bongu, Q. Bao, N.C. Panouli, Nonlinear optical properties and applications of 2D materials: theoretical and experimental aspects, *Nanophotonics* 8 (2018) 63–97.
- S.P. Kamble, V.D. Mote, Optical and room-temperature ferromagnetic properties of Ni-doped CuO nanocrystals prepared via auto-combustion method, *J. Mater. Sci. Mater. Electron.* 32 (2021) 5309–5315, <https://doi.org/10.1007/s10854-020-05106-8>.
- H. van Gog, W.F. Li, C. Fang, R.S. Koster, M. Dijkstra, M. van Huis, Thermal stability and electronic and magnetic properties of atomically thin 2D transition metal oxides, *npj 2D Mater. Appl.* 3 (2019) 1–13, <https://doi.org/10.1038/s41699-019-0100-z>.
- K. Jiang, P. Xiong, J. Ji, J. Zhu, R. Ma, T. Sasaki, F. Geng, Two-dimensional molecular sheets of transition metal oxides toward wearable energy storage, *Acc. Chem. Res.* 53 (2020) 2443–2455, <https://doi.org/10.1021/acs.accounts.0c00483>.
- B. Jaber, N. Zayyoun, L. Bahmad, L. Laa, The Effect of pH on the Synthesis of Stable Cu₂O/CuO Nanoparticles by Sol – Gel Method in A Glycolic Medium, 2016, pp. 3–8. (<https://doi.org/10.1007/s00339-016-0024-9>).
- V. Usha, S. Kalyanaraman, R. Thangavel, R. Vettumperumal, Effect of catalysts on the synthesis of CuO nanoparticles: structural and optical properties by sol-gel method, *Superlattices Microstruct.* (2015), <https://doi.org/10.1016/j.spmi.2015.07.053>.
- J. Meng, G. Liu, W. Zhang, L. Zhao, H. Liu, X. Jia, D. Mu, S. Liu, X. Dong, J. Zhang, W. Lu, G. Wang, Y. Zhou, Y. Zhu, X. Wang, Z. Xu, C. Chen, X.J. Zhou, Coexistence of Fermi arcs and Fermi pockets in a high-T(c) copper oxide superconductor, *Nature* 462 (2009) 335–338, <https://doi.org/10.1038/nature08521>.
- B.P. Singh, M. Chaudhary, A. Kumar, A.K. Singh, Y.K. Gautam, S. Rani, R. Walia, Effect of Co and Mn doping on the morphological, optical and magnetic properties of CuO nanostructures, *Solid State Sci.* 106 (2020), 106296, <https://doi.org/10.1016/j.solidstatesciences.2020.106296>.
- A. Kumar, M. Kumar, P. Chandra Sati, M.K. Srivastava, S. Ghosh, S. Kumar, Structural, magnetic and optical properties of diluted magnetic semiconductor (DMS) phase of Ni modified CuO nanoparticles, *Curr. Appl. Phys.* 32 (2021) 24–35, <https://doi.org/10.1016/j.cap.2021.09.002>.
- D.M. Jundale, P.B. Joshi, S. Sen, V.B. Patil, Nanocrystalline CuO thin films: synthesis, microstructural and optoelectronic properties, *J. Mater. Sci. Mater. Electron.* 23 (2012) 1492–1499, <https://doi.org/10.1007/s10854-011-0616-2>.
- G. Avgouropoulos, T. Ioannides, Effect of synthesis parameters on catalytic properties of CuO-CeO₂, *Appl. Catal. B Environ.* 67 (2006) 1–11, <https://doi.org/10.1016/j.apcatb.2006.04.005>.
- C. Thangamani, M. Ponnar, P. Priyadarshini, P. Monisha, S.S. Gomathi, K. Pushpanathan, Magnetic behavior of Ni Doped CuO nanoparticles synthesized by microwave irradiation method, *Surf. Rev. Lett.* 26 (2019) 1850184.
- S.M. Jabbar, Synthesis of CuO Nano Structure via Sol-Gel and Precipitation Chemical Methods, 12, 2018, pp. 126–131.
- S.R. Zohra Nazir Kayani, Maryam Umer, S. Naseem, Characterization of copper oxide nanoparticles fabricated by the sol-gel method, *J. Electron. Mater.* 44 (2015) 3704–3709.
- H. Khmissi, A.M. El Sayed, M. Shaban, Structural, morphological, optical properties and wettability of spin-coated copper oxide; influences of film thickness, Ni, and (La, Ni) co-doping, *J. Mater. Sci.* (2016), <https://doi.org/10.1007/s10853-016-9894-7>.
- J.Y. Xiang, J.P. Tu, L. Zhang, Y. Zhou, X.L. Wang, S.J. Shi, Self-Assembled Synthesis of Hierarchical Nanostructured CuO with Various Morphologies and Their Application as Anodes for Lithium Ion Batteries, 195, 2010, pp. 313–319. (<https://doi.org/10.1016/j.jpowsour.2009.07.022>).
- A. Chen, G. Yang, H. Long, P. Lu, W. Zhang, H. Wang, Optical limiting properties in copper oxide thin films under a high-repetition-rate femtosecond laser, *Mater. Lett.* 91 (2013) 319–322, <https://doi.org/10.1016/j.matlet.2012.09.111>.
- K. Velsankar, R.M.A. Kumar, R. Preeti, V. Muthulakshmi, S. Sudhahar, *Biochem. Pharm.* (2020), 104123, <https://doi.org/10.1016/j.jece.2020.104123>.
- J.H. Miao, S.L. Yuan, L. Yuan, G.M. Ren, X. Xiao, G.Q. Yu, Y.Q. Wang, S.Y. Yin, Giant magnetoresistance in La_{0.67}Ca_{0.33}MnO₃ granular system with CuO addition, *Mater. Res. Bull.* 43 (2008) 631–638, <https://doi.org/10.1016/j.materresbull.2007.04.006>.
- H. Kidowaki, T. Oku, T. Akiyama, A. Suzuki, B. Jeyadevan, J. Cuya, Fabrication and characterization of CuO-based solar cells, *J. Mater. Sci. Res* 1 (2011), <https://doi.org/10.5539/jmsr.v1n1p138>.
- C. Te Hsieh, J.M. Chen, H.H. Lin, H.C. Shih, Field emission from various CuO nanostructures, *Appl. Phys. Lett.* 83 (2003) 3383–3385, <https://doi.org/10.1063/1.1619229>.
- J.D. Rodney, S. Deepapriya, M. Cyril Robinson, C. Justin Raj, S. Perumal, B.C. Kim, S. Jerome Das, Lanthanum doped copper oxide nanoparticles enabled proficient bifunctional electrocatalyst for overall water splitting, *Int. J. Hydrog. Energy* 45 (2020) 24684–24696, <https://doi.org/10.1016/j.ijhydene.2020.06.240>.
- G.S. Boltsev, R.A. Ganeev, P.S. Krishnendu, K. Zhang, C. Guo, Nonlinear optical characterization of copper oxide nanoellipsoids, *Sci. Rep.* (2019) 1–8, <https://doi.org/10.1038/s41598-019-47941-8>.
- B. Karthikeyan, Raman spectral probed electron – phonon coupling and phonon lifetime properties of Ni - doped CuO nanoparticles, *Appl. Phys. A* 127 (2021) 1–7, <https://doi.org/10.1007/s00339-021-04330-1>.
- M. Chandrasekar, M. Subash, S. Logambal, G. Udhayakumar, R. Uthrakumar, C. Imozhi, W.A. Al-onazi, A.M. Al-mohaimed, T. Chen, K. Kanimozhi, Synthesis and characterization studies of pure and Ni doped CuO nanoparticles by hydrothermal method, *J. King Saud. Univ. Sci.* 34 (2022), 101831, <https://doi.org/10.1016/j.jksus.2022.101831>.
- C. Thangamani, M. Ponnar, P. Priyadarshini, P. Monisha, S.S. Gomathi, K. Pushpanathan, Magnetic behavior of Ni-doped CuO nanoparticles synthesized by microwave irradiation method, *Surf. Rev. Lett.* 26 (2019), <https://doi.org/10.1142/S0218625x18501846>.
- J. Ha, J. Oh, H. Choi, H. Ryu, W. Lee, J. Bae, Photoelectrochemical properties of Ni-doped CuO nanorods grown using the modified chemical bath deposition method, *J. Ind. Eng. Chem.* 58 (2018) 38–44, <https://doi.org/10.1016/j.jiec.2017.09.004>.
- N.M. Basith, J.J. Vijaya, L.J. Kennedy, M. Bououidina, Structural, morphological, optical, and magnetic properties of Ni-doped CuO nanostructures prepared by a rapid microwave combustion method, *Mater. Sci. Semicond. Process.* 17 (2014) 110–118, <https://doi.org/10.1016/j.mssp.2013.09.013>.
- C. Thangamani, M. Ponnar, P. Priyadarshini, P. Monisha, S.S. Gomathi, K. Pushpanathan, Magnetic behavior of Ni Doped CuO nanoparticles synthesized by microwave irradiation method, *Surf. Rev. Lett.* 36 (2019) 1850184, <https://doi.org/10.1142/S0218625x18501846>.
- S. Dolai, S.N. Sarangi, S. Hussain, R. Bhar, A.K. Pal, Magnetic properties of nanocrystalline nickel incorporated CuO thin films, *J. Magn. Magn. Mater.* 479 (2019) 59–66, <https://doi.org/10.1016/j.jmmm.2019.02.005>.
- H.H. Huang, F.Q. Yan, Y.M. Kek, C.H. Chew, G.Q. Xu, W. Ji, P.S. Oh, S.H. Tang, Synthesis, characterization, and nonlinear optical properties of copper nanoparticles, *Langmuir* 13 (1997) 172–175.
- M. Shahmiri, N. Azowa, N. Faraji, W. Mahmood, M. Yunus, Third-order nonlinear optical properties of chemically synthesized copper oxide nanosheets, *Phys. E Low-Dimens. Syst. Nanostruct.* 54 (2013) 109–114, <https://doi.org/10.1016/j.physe.2013.06.014>.
- L.V. Devi, T. Selvalakshmi, S. Sellaiyan, A. Uedono, K. Sivaji, S. Sankar, Effect of La doping on the lattice defects and photoluminescence properties of CuO, *J. Alloy. Compd.* 709 (2017) 496–504, <https://doi.org/10.1016/j.jallcom.2017.03.148>.
- A. Kumar, M. Kumar, P. Chandra, M. Kumar, S. Ghosh, S. Kumar, Structural, magnetic and optical properties of diluted magnetic semiconductor (DMS) phase of Ni modified CuO nanoparticles, *Curr. Appl. Phys.* 32 (2021) 24–35, <https://doi.org/10.1016/j.cap.2021.09.002>.
- H.G. Gebretinsae, M.G. Tsegay, Z.Y. Nuru, Biosynthesis of nickel oxide (NiO) nanoparticles from cactus plant extract, *Mater. Today Proc.* (2020), <https://doi.org/10.1016/j.matpr.2020.05.331>.
- M. Arfan, D. Nawaid, T. Shahid, Z. Iqbal, Y. Majeed, I. Akram, R. Bagheri, Z. Song, A. Zeb, Tailoring of nanostructures: Al doped CuO synthesized by composite-hydroxide-mediated approach, *Results Phys* (2019), 102187, <https://doi.org/10.1016/j.rinp.2019.102187>.
- S. Kamila, V.R. Venugopal, Synthesis and Structural Analysis of Different CuO Nano Particles, 2017, pp. 133–146. ([https://doi.org/10.6703/IJASE.2017.14\(3\).133](https://doi.org/10.6703/IJASE.2017.14(3).133)).
- P. Mallick, S. Sahu, Structure, Microstructure and Optical Absorption Analysis of CuO Nanoparticles Synthesized by Sol-Gel Route, 2, 2012, pp. 71–74. (<https://doi.org/10.5923/j.nn.20120203.05>).
- V.U. Siddiqui, A. Ansari, M.T. Ansari, K. Akram, Optimization of facile synthesized ZnO/CuO nanophotocatalyst for organic dye degradation by visible light irradiation using response surface methodology, *Catalysts* 15 (2021) 1509.
- S.R.G. Viruthagiri, R.G.N. Shanmugam, Synthesis and characterization of Ni 2 + ions incorporated CuO nanoparticles and its application in antibacterial activity, *J. Mater. Sci. Mater. Electron.* 27 (2016) 2701–2711, <https://doi.org/10.1007/s10854-015-4080-2>.
- H. Li, Y. Sun, F. Chang, H. Deng, L. Xie, H. Li, High sensitive gas sensor based on CuO nanoparticles synthesized by sol-gel method, *R. Soc. Chem.* 6 (2013) 79343–79349, <https://doi.org/10.1039/C6RA13876D>.

- [42] S. Nithya, R. Sharan, M. Roy, H. Ho, T. Ishihara, A. Dutta, Ni doping in CuO: A highly sensitive electrode for sensing ammonia in ppm level using lanthanum gallate based electrolyte, *Mater. Res. Bull.* 118 (2019), 110478, <https://doi.org/10.1016/j.materresbull.2019.05.003>.
- [43] A. Bhaumika, A.M. Shearina, R. Patela, K. Ghosh, Significant enhancement of optical absorption through nano structuring of copper based oxide semiconductors: possible future materials for solar energy applications, *Phys. Chem. Chem. Phys.* 16 (2014) 11054–11066.
- [44] T. Jan, S. Azmat, Q. Mansoor, S.Z. Ilyas, I. Ahmad, H. Khan, M. Ismail, Structural, Raman, optical and novel antibacterial characteristics of Al doped CuO nanostructures, *Mater. Res. Express* (2019) 1–10, <https://doi.org/10.1088/2053-1591/ab3f8c>.
- [45] S. Al-amri, M.S. Ansari, S. Rafique, M. Aldahri, Ni Doped CuO Nanoparticles: Structural and Optical Characterizations, 2015. (<https://doi.org/10.2174/1573413710666141024212856>).
- [46] H. Siddiqui, M. Ramzan, P. Fozia, Optimization of process parameters and its effect on structure and morphology of CuO nanoparticle synthesized via the sol – gel technique, *J. Sol-Gel Sci. Technol.* (2018), <https://doi.org/10.1007/s10971-018-4663-5>.
- [47] J.F. Xu, W. Ji, Z.X. Shen, W.S. Li, S.H. Tang, X.R. Ye, D.Z. Jia, X.Q. Xin, Raman Spectra of CuO Nanocrystals, 415, 1999, pp. 413–415.
- [48] L.V. Devi, T. Selvalakshmi, S. Sellaiyan, A. Uedono, K. Sivaji, S. Sankar, Effect of La doping on the lattice defects and photoluminescence properties of CuO, *J. Alloy. Compd.* 709 (2017) 496–504, <https://doi.org/10.1016/j.jallcom.2017.03.148>.
- [49] B. Arunkumar, S. Johnson Jeyakumar, M. Jothibas, A sol-gel approach to the synthesis of CuO nanoparticles using Lantana camara leaf extract and their photo catalytic activity, *Optik* 183 (2019) 698–705, <https://doi.org/10.1016/j.ijleo.2019.02.046>.
- [50] S.M. Jabbar, Synthesis of CuO nano structure via sol-gel and precipitation chemical methods, *Al-Khwarizmi Eng. J.* 12 (2017) 126–131, <https://doi.org/10.22153/kej.2016.07.001>.
- [51] A.A. Radhakrishnan, B.B. Beena, Structural and optical absorption analysis of CuO nanoparticles, *Indian J. Adv. Chem. Sci.* 2 (2014) 158–161.
- [52] V. Usha, S. Kalyanaraman, R. Thangavel, R. Vettumperumal, Effect of catalysts on the synthesis of CuO nanoparticles: structural and optical properties by sol-gel method, *Superlattices Microstruct.* 86 (2015) 203–210, <https://doi.org/10.1016/j.spmi.2015.07.053>.
- [53] J. Jayaprakash, N. Srinivasan, P. Chandrasekaran, Surface modifications of CuO nanoparticles using ethylene diamine tetra acetic acid as a capping agent by sol-gel routine, *Spectrochim. Acta Part A Mol. Biomol. Spectrosc.* 123 (2014) 363–368.
- [54] S.K. Kuanr, S. Nayak, K.S. Babu, Ni dependent structural, optical and electrical properties of CuO nanostructures, *Mater. Sci. Semicond. Process.* 71 (2017) 268–274, <https://doi.org/10.1016/j.mssp.2017.08.012>.
- [55] S. Baturay, A. Tombak, D. Kaya, Y.S. Ocak, M. Tokus, M. Aydemir, T. Kilicoglu, Modification of electrical and optical properties of CuO thin films by Ni doping, *J. Sol-Gel Sci. Technol.* 78 (2016) 422–429, <https://doi.org/10.1007/s10971-015-3953-4>.
- [56] H. Siddiqui, M.R. Parra, Studies of structural, optical, and electrical properties associated with defects in sodium-doped copper oxide (CuO / Na) nanostructures, *J. Mater. Sci.* 53 (2018) 8826–8843, <https://doi.org/10.1007/s10853-018-2179-6>.
- [57] P. Chand, A. Gaur, A. Kumar, Structural, optical and ferroelectric behavior of CuO nanostructures synthesized at different pH values, *Superlattices Microstruct.* 60 (2013) 129–138, <https://doi.org/10.1016/j.spmi.2013.04.026>.
- [58] X. Zhao, P. Wang, Z. Yan, N. Ren, Room temperature photoluminescence properties of CuO nanowire arrays, *Opt. Mater.* (2015) 10–13, <https://doi.org/10.1016/j.optmat.2014.12.032>.
- [59] M. Sheik-bahae, A.L.I.A. Said, T. Wei, Sensitive Measurement of Optical Nonlinearities Using a Single Beam, 26, 1990.
- [60] K.A.A. Mary, N.V. Unnikrishnan, R. Philip, Role of Surface States and Defects in the Ultrafast Nonlinear Optical Properties of CuS Quantum Dots, 076104, 2017. (<http://doi.org/10.1063/1.4886276>).
- [61] H.S. Sindhu, S.R. Maidur, P. Shankaragouda, Optik Nonlinear optical and optical power limiting studies of Zn 1-x Mn x O thin films prepared by spray pyrolysis, *Opt. Int. J. Light Electron Opt.* 182 (2019) 671–681, <https://doi.org/10.1016/j.ijleo.2019.01.031>.
- [62] R. Divya, N. Manikandan, G. Vinitha, Synthesis and characterization of nickel doped zinc selenide nanospheres for nonlinear optical applications, *J. Alloy. Compd.* 791 (2019) 601–612, <https://doi.org/10.1016/j.jallcom.2019.03.294>.
- [63] U. Vinoditha, B.K. Sarojini, K.M. Sandeep, B. Narayana, S.R. Maidur, P.S. Patil, K. M. Balakrishna, Defects-induced nonlinear saturable absorption mechanism in europium-doped ZnO nanoparticles synthesized by facile hydrothermal method, *Appl. Phys. A Mater. Sci. Process.* 125 (2019) 1–11, <https://doi.org/10.1007/s00339-019-2732-4>.
- [64] V. Siva, S.A. Bahadur, A. Shameem, S. Athimoolam, K.U. Lakshmi, G. Vinitha, Synthesis, structural, vibrational, thermal, dielectric and optical properties of third order nonlinear optical single crystal for optical power limiting applications, *J. Mol. Struct.* 1191 (2019) 110–117, <https://doi.org/10.1016/j.molstruc.2019.04.091>.
- [65] Y.S. Tamgadge, V.G. Pahrkar, S.S. Talwatkar, A.L. Sunatkari, G.G. Muley, Thermally stimulated third - order optical nonlinearity in Cd - doped CuO – PVA thin films under cw laser illumination, *Appl. Phys. B* (2015), <https://doi.org/10.1007/s00340-015-6147-4>.
- [66] Gananatha Shetty B, Vincent Crasta, Rithin Kumar N B, Rajesh K, Raghavendra Bairy, Parutagouda Shankaragouda Patile, Promising PVA / TiO2, CuO filled Nanocomposites for Electrical and Third Order Nonlinear Optical Applications, 95, 2019. (<https://doi.org/10.1016/j.optmat.2019.109218>).
- [67] Y.S. Tamgadge, S.S. Talwatkar, A.L. Sunatkari, V.G. Pahrkar, G.G. Muley, Studies on nonlocal optical nonlinearity of Sr – CuO – polyvinyl alcohol nanocomposite thin films, *Thin Solid Films* 595 (2015) 48–55, <https://doi.org/10.1016/j.tsf.2015.10.039>.
- [68] S.R. Tuhin Maity, Sudipta Goswami, Dipten Bhattacharya, Superspin glass mediated giant spontaneous exchange bias in a nanocomposite of BiFeO3-Bi2Fe4O9, *Phys. Rev. Lett.* 110 (2013), 107201.